

Weighted Regularization in Electrical Impedance Tomography With Applications to Acute Cerebral Stroke

M. T. Clay and T. C. Ferree*

Abstract—We apply electrical impedance tomography to detect and localize brain impedance changes associated with stroke. Forward solutions are computed using the finite-element method in two dimensions. We assume that baseline conductivity values are known for the major head tissues, and focus on changes in the brain compartment only. We use singular-value decomposition (SVD) to show that different impedance measurement patterns, which are theoretically equivalent by the reciprocity theorem, have different sensitivities to the brain compartment in the presence of measurement noise. The inverse problem is solved in part by standard means, using iterated SVD, and regularizing by truncation. To improve regularization we introduce a weighting scheme which normalizes the sensitivity matrix for voxels at different depths. This increases the number of linearly independent components which contribute to the solution, and forces the different measurement patterns to have similar sensitivity. When applied to stroke, this weighted regularization improves image quality overall.

Index Terms—Conductivity, finite-element, impedance tomography, regularization, stroke.

I. INTRODUCTION

ELECTRICAL impedance tomography (EIT) is a noninvasive method for determining the conductivity distribution inside a volume, based upon four-electrode impedance measurements taken at the surface. This is useful for making forward models in any bioelectromagnetic imaging application, including electrocardiography (ECG) [8], electroencephalography (EEG) [2], [10], and magnetoencephalography (MEG) [17]. In addition, changes in local tissue impedance reflect a variety of pathologies, making EIT useful clinically [28].

When EIT is applied to the thorax, e.g., to determine tissue conductivities for ECG [8], the injected current passes relatively unhindered between the ribs. Even so, the inverse problem of constructing volumetric images from surface measurements is mathematically ill-posed and computationally very demanding

[7]. When EIT is applied to the head, the inverse problem becomes even more ill-posed due to the presence of the poorly conducting skull [28].

In this paper we address the problem of acute cerebral stroke detection and monitoring. We consider both types of cerebral stroke: ischemic and hemorrhagic. Ischemic stroke occurs when blood flow is reduced, e.g., due to a clogged artery. The most common technique for imaging stroke is magnetic resonance imaging (MRI). However, while conventional MRI shows infarcted (dead) tissue many hours after stroke onset, it cannot readily detect ischemic tissue in the acute time window (i.e., within three hours), in which tissue may be rescuable by drug intervention. New MRI techniques such as diffusion tensor imaging hold promise [3], but no MRI device is yet practical for mobile use or continuous bedside monitoring.

Ischemic tissue is characterized by anomalously high impedance. This occurs because of cell swelling, which reduces the extracellular space, and increases the bulk tissue impedance by as much as 50% [16], [20]. The utility of EIT for detecting ischemia has been demonstrated experimentally in rodents [20], [21]. In humans, ischemic tissue also generates pathological EEG and MEG [22], [31]. The work presented here was motivated in part by the recognition that EIT data could easily be acquired concurrently with EEG, e.g., in mobile units or during continuous brain monitoring in the intensive care unit, and provide complementary information on brain state.

A related problem is hemorrhagic stroke, which occurs when blood fills the extracellular space or displaces brain tissue entirely. While far fewer patients present with hemorrhagic stroke, it is much more likely to result in death. Ironically, the primary drug used to treat cerebral ischemia (t-PA) carries a 6% chance of causing brain hemorrhage [1]. Since the conductivity of blood ($\sigma_b = 0.61$ S/m) [12] is approximately four times that of brain ($\sigma_h = 0.15$ S/m), it seems possible to detect hemorrhagic stroke with EIT as well.

EIT in the head is obviously challenged by the low skull conductivity, since much of the current is shunted through the scalp and does not enter the brain compartment [28], [37]. Nevertheless, recent studies have applied EIT to measure functional brain activity in humans [39], [40], involving relatively small conductivity changes. In this paper, we use computer simulations to investigate how well EIT might detect ischemic and hemorrhagic stroke in humans.

Three aspects of the present approach have direct bearing on the results. First, we assume that head geometry is known, since

Manuscript received August 4, 2001; revised May 17, 2002. This work was supported in part by National Institutes of Health (NIH) under Grant R43-NS-38788 and Grant R44-NS-38829. *Asterisk indicates corresponding author.*

M. T. Clay is with the Electrical Geodesics, Inc., Eugene, OR 97403 USA. He is also with the Department of Mathematics, University of Oregon, Eugene, OR 97403 USA.

*T. C. Ferree is with the Electrical Geodesics, Inc., Riverfront Research Park, Eugene, OR 97403 USA and the Computational Science Institute, University of Oregon, Eugene, OR 97403 USA. He is now with the Dynamic Neuroimaging Laboratory, Department of Radiology, University of California, San Francisco, CA 94143 USA.

Publisher Item Identifier 10.1109/TMI.2002.800572.

this data can be obtained from structural MRI, or potentially from anatomical databases. Second, we adopt the most reliable estimate of average skull conductivity available [32]. Third, to focus on *changes* in brain conductivity which might occur in stroke, we fix the conductivity of the outer head tissues [scalp, skull, and cerebrospinal fluid (CSF)] to baseline values. These may be obtained as in [10], or using other methods suggested below.

In solving the EIT inverse problem, we use a standard iterative approach for the nonlinear aspect [30], and invert the sensitivity matrix using singular-value decomposition (SVD). The SVD implements regularization by truncation [35], and has been used previously in EIT [39], [40]. To the regularization procedure, we further introduce a matrix weighting, or preconditioning, scheme which normalizes the sensitivity matrix for different depths. This weighting scheme has been applied previously in geophysics [34] and EEG/MEG [15], but to our knowledge has not been applied previously to the EIT inverse problem. By analyzing the singular values, rank, and condition of the sensitivity matrix, we show that weighting increases the number of linearly independent measurements which contribute to the solution, forces the different EIT injection patterns to have similar sensitivity, and improves image reconstruction quality overall.

II. THEORY

A. Forward Problem

Low-frequency ($f < 10$ kHz) current injected into the scalp gives rise to quasistatic electric fields, which may be computed using techniques from electrostatics. To a good approximation, the electric and magnetic fields are decoupled and the local tissue impedance is real [33]. The “impressed” current passes primarily through the extracellular space [11], and is kept low ($I_{inj} < 100 \mu\text{A}$ injected at the scalp surface) so as not to elicit neural activity.

With these simplifications, electric current in the conductive media is governed by Poisson’s equation for the electric potential Φ subject to Neumann boundary conditions

$$\vec{\nabla} \cdot (\sigma \vec{\nabla} \Phi) = 0 \quad \text{in } \Omega \quad (1)$$

$$\frac{\partial \Phi}{\partial \nu} = -\frac{J_{\perp}}{\sigma} \quad \text{on } \partial\Omega \quad (2)$$

where $\vec{\nabla} \equiv (\partial/\partial x, \partial/\partial y, \partial/\partial z)$ is the three-dimensional (3-D) gradient and $\sigma(x, y, z)$ is the local tissue conductivity. The volume Ω is bounded by the surface $\partial\Omega$ with outward unit normal $\hat{\nu}$. The normal current density at the scalp-air boundary $J_{\perp} \equiv \vec{J} \cdot \hat{\nu}$ is specified piecewise; it is nonzero only at the electrodes. Equation (1) reduces to Laplace’s equation ($\nabla^2 \Phi = 0$) in each tissue layer, if σ is piecewise constant.

B. Reduction to Two Dimensions

It is common in the literature to use approximate two-dimensional (2-D) models as a starting point for investigation, since their solution is simpler mathematically, faster computationally, and easier to visualize. Physically, the current always flows in three dimensions, but when EIT is applied to the thorax, both injection and measurement electrodes are commonly confined to a plane [28] to simplify the problem. We acknowledge that 2-D

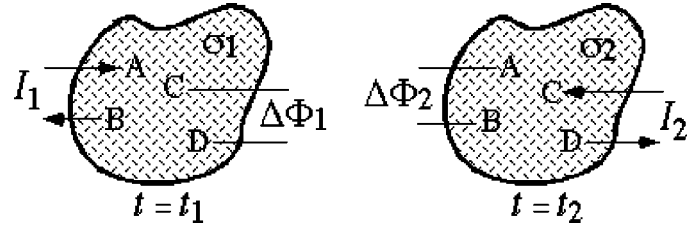


Fig. 1. Configurations relevant to the four-electrode reciprocity theorem [19].

models are not completely satisfactory for real applications, but we use a 2-D model here as a first step. To clarify its interpretation, we note its mathematical relationship to a class of 3-D models exhibiting translational symmetry.

If the volumetric conductivity has translational symmetry along some axis, e.g., the z axis so that $\sigma = \sigma(x, y)$, then the solution to (1) in two dimensions may be put into relation with a corresponding 3-D problem as follows. For an object of height L , separation of variables [23] allows the solution to Laplace’s equation ($\nabla^2 \Phi = 0$) to be written as

$$\Phi(x, y, z) = \sum_{k=0}^{\infty} \phi_k(x, y) \cos\left(\frac{k\pi}{L} z\right) \quad (3)$$

where $z \in [0, L]$. Inserting (3) into (1) and using $\sigma = \sigma(x, y)$ leads to an equation for each $\phi_k(x, y)$

$$\vec{\nabla}_2 \cdot (\sigma \vec{\nabla}_2 \phi_k) - \sigma \left(\frac{k\pi}{L}\right)^2 \phi_k = 0 \quad (4)$$

where $\vec{\nabla}_2 \equiv (\partial/\partial x, \partial/\partial y)$ is the 2-D gradient operator. We used Cartesian coordinates in (3), but (4) also holds in cylindrical coordinates if $\phi_k(x, y) \rightarrow \psi_k(r, \theta)$.

Equation (4) shows that by solving (1) in two dimensions, only the $k = 0$ contribution to (3) is obtained. Most 3-D problems of interest have no exact symmetry, so any 2-D results are only approximate. Yet numerical evidence suggests that the EIT problems in 2-D and axially symmetric 3-D geometry are similarly ill-posed [25], so the numerical findings of the present study may be expected to extend well to three dimensions.

C. Reciprocity Formulation

Our starting point for EIT is the Geselowitz–Lehr theorem [14], [27] relating *changes* in local conductivity to changes in surface potential. Fig. 1 shows the four-electrode measurement configuration. Obviously, we must require $A \neq B$ and $C \neq D$. At time t_1 (t_2), the conductivity is a scalar field σ_1 (σ_2). Current I_1 (I_2) is passed through a pair of electrodes AB (CD), setting up an electric potential field Φ_1 (Φ_2) throughout the volume. The potential difference measured across the pair {CD} ({AB}) is denoted $\Delta\Phi_1$ ($\Delta\Phi_2$). Due to well-known practical problems with measuring and computing the potential at the injection electrodes, it is usually assumed that pairs {AB} and {CD} share no electrodes [18]. For convenience, it is also assumed that $I_1 = I_2$.

Applying techniques like those used to derive Green’s second theorem [14], [27] to the products $\Phi_1 \vec{J}_2$ and $\Phi_2 \vec{J}_1$, it may be shown that

$$Z_2 - Z_1 = - \int_{\Omega} \Delta\sigma \vec{L}_1(\sigma_1) \cdot \vec{L}_2(\sigma_2) d\Omega \quad (5)$$

where the mutual impedance $Z_i \equiv \Phi_i/I_i$, the change in conductivity $\Delta\sigma \equiv \sigma_2 - \sigma_1$, and the lead field vector $\vec{L}_i \equiv -\vec{\nabla}\Phi_i/I_i$. If the change $\Delta\sigma$ represents an actual change in the volume from t_1 to t_2 , then this forward expression is exact.

D. Iterative Nonlinear Solution

Equation (5) is nonlinear in $\Delta\sigma$ by its presence in $L_2(\sigma_1 + \Delta\sigma)$. This may be handled iteratively [30]. The first step is to assume that $\Delta\sigma$ is in some sense “small,” making it valid to linearize the dependence on $\Delta\sigma$

$$Z_2 - Z_1 \simeq - \int_{\Omega} \Delta\sigma \vec{L}_1(\sigma_1) \cdot \vec{L}_2(\sigma_1) d\Omega. \quad (6)$$

Following [30], we seek an iterative solution to the nonlinear problem (5) via the linear problem (6), in which our estimate for σ evolves according to a discrete map: $\sigma^{(n+1)} = \sigma^{(n)} + \Delta\sigma^{(n)}$, where n is the iteration step. Such a map is useful if it leads to an estimate of σ which minimizes the difference between measured and computed impedances Z . At that point $\sigma_1 = \sigma_2$ and the solution of (6) approaches that of (5).

A slight reinterpretation of (6) gives an iterative algorithm for computing the conductivity field σ which has minimum least-squares error relative to the measured impedances Z^* . We first define a measurement μ in terms of four distinct electrodes: $\mu = \{\text{AB}; \text{CD}\}$, corresponding to t_1 in Fig. 1. On the right-hand side of (6), we take “1” and “2” to be two successive theoretical estimates of σ , written $\sigma^{(n)}$ and $\sigma^{(n+1)}$. On the left side, the mutual impedance Z_1 is replaced by $Z_{\mu}^{(n)}$, the computed value of Z for measurement μ at iteration step n , and Z_2 is replaced by Z_{μ}^* , the measured value of Z for the same μ . We thus have

$$Z_{\mu}^* - Z_{\mu}^{(n)} \simeq - \int_{\Omega} (\sigma^{(n+1)} - \sigma^{(n)}) H_{\mu}^{(n)} d\Omega \quad (7)$$

where the density $H_{\mu}^{(n)} \equiv \vec{L}_{\text{AB}}(\sigma^{(n)}) \cdot \vec{L}_{\text{CD}}(\sigma^{(n)})$.

The finite-element method (FEM) discretizes the problem domain Ω into small volume elements Ω_k called voxels. This allows the integral in (7) to be replaced by a sum. The conductivity σ is assumed constant over each voxel, while the potential Φ varies linearly over each voxel [30]. This allows (7) to be written

$$Z_{\mu}^* - Z_{\mu}^{(n)} \simeq \sum_{k=1}^N S_{\mu k}^{(n)} (\sigma_k^{(n+1)} - \sigma_k^{(n)}) \quad (8)$$

where voxels are indexed by $k \in [1, N]$. The sensitivity matrix $S_{\mu k}^{(n)}$ is defined

$$S_{\mu k}^{(n)} \equiv - \int_{\Omega_k} H_{\mu}^{(n)} d\Omega. \quad (9)$$

This linear formulation is only approximate, valid for small $\Delta\sigma$. Moreover, $S_{\mu k}^{(n)}$ tends to be singular, so that the corresponding inverse problem of solving (8) for $\Delta\sigma_k^{(n)}$ is ill-posed and requires regularization.

Given an approximate solution to the linear inverse problem (8) for each n , e.g., via the Moore–Penrose pseudoinverse S^+ described next, the solution to the original nonlinear problem may be obtained by iterating [30]

$$\sigma_k^{(n+1)} = \sigma_k^{(n)} + \eta \sum_{\mu=1}^M (S^+)^{(n)}_{k\mu} [Z_{\mu}^* - Z_{\mu}^{(n)}] \quad (10)$$

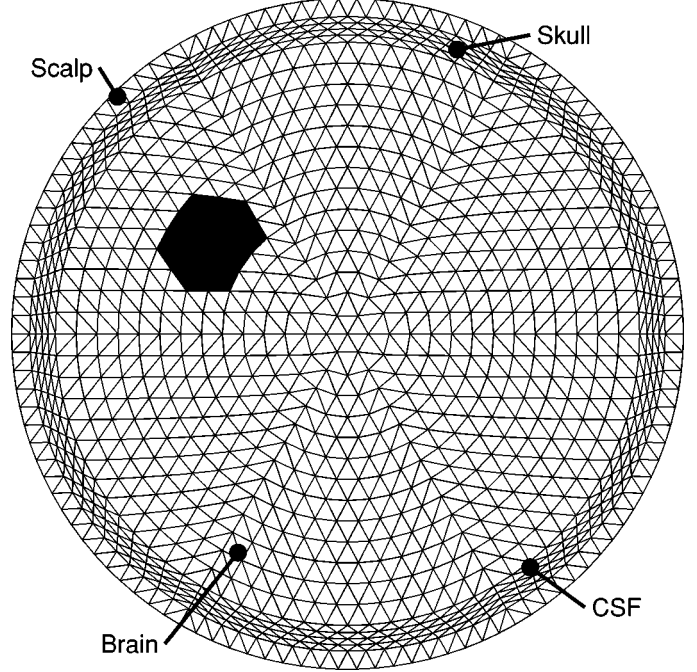


Fig. 2. FE mesh consisting of 1141 nodes and 2166 elements. The brain compartment alone has 1176 elements. Outer radii are equal to 8.0 cm (brain), 8.2 cm (CSF), 8.7 cm (skull), and 9.2 cm (scalp). These values are considered typical [10]. The dark area shows an impedance anomaly located in Region 3.

where the parameter $\eta \in (0, 1]$ is introduced *ad hoc* to improve convergence [35]. The choice of such parameters is typically subjective and problem dependent [34]. The value $\eta = 0.33$ worked well for this problem.

Our algorithm stops when either of the two convergence criteria are satisfied. First, if the Euclidean norm of the conductivity step becomes less than some tolerance, i.e.,

$$\|\sigma^{(n+1)} - \sigma^{(n)}\| < 10^{-3} \quad \text{S/m} \quad (11)$$

then the minimization procedure is presumed to have reached a local minimum. Second, if the mutual impedance change is less than some tolerance, i.e.,

$$\frac{1}{M} \sum_{\mu=1}^M (Z_{\mu}^{(n+1)} - Z_{\mu}^{(n)})^2 < \rho \delta V^2 \quad (12)$$

then the result is said to no longer be changing with adequate signal-to-noise ratio. Here, δV is the voltage measurement noise level discussed below, and ρ is a normalization parameter described in [34]. In this study, these two criteria acted similarly to terminate the search after approximately 30 steps.

E. Regularization Via SVD

We assume a finite number M of measurements Z_{μ}^* , where $\mu \in [\mu_1, \dots, \mu_M]$. The problem of inverting (8) for the vector $\Delta\sigma_k^{(n)}$, the so-called tomographic reconstruction problem, is ill-posed, primarily because $M \ll N$, which makes $S_{\mu k}^{(n)}$ singular [45]. For the mesh in Fig. 2, this is improved somewhat by assuming the outer tissues (scalp, skull, and CSF) are known and fixed, but still $M < N$. Even if $M \geq N$, the EIT inverse problem is generally ill-posed, i.e., $S_{\mu k}^{(n)}$ remains singular, due to instrument noise and the blurring nature of the volume conductor. In this paper, we use the method of SVD to regularize

the inverse problem, and obtain a solution with minimum error $\|Z^* - Z^{(n)}\|$ and minimum norm $\|\Delta\sigma^{(n)}\|$, where $\|\cdot\|$ denotes the L_2 norm [39], [40].

At each iteration step n , the linear system (8) may be expressed in matrix notation as

$$\Delta\mathbf{Z} = \mathbf{S}\Delta\sigma. \quad (13)$$

This system of equations may be solved approximately for $\Delta\sigma$ using the SVD method [24], [35]. Briefly, any matrix \mathbf{S} may be decomposed as $\mathbf{S} = \mathbf{U}\mathbf{\Lambda}\mathbf{V}^T$, where $\mathbf{\Lambda} = \text{diag}(\lambda_m)$, i.e., $\mathbf{\Lambda}$ is the diagonal matrix constructed from the ordered set of M singular values λ_m , and \mathbf{U} and \mathbf{V} are orthogonal matrices constructed from the left and right eigenvectors of \mathbf{S} . This decomposition allows an approximate solution to be written

$$\Delta\sigma \simeq \mathbf{S}^+ \Delta\mathbf{Z} \quad (14)$$

where \mathbf{S}^+ represents the Moore–Penrose pseudoinverse, given by $\mathbf{S}^+ = \mathbf{V}\mathbf{\Lambda}^+\mathbf{U}^T$ [24]. The key to its utility is that $\mathbf{\Lambda}^+$ denotes the pseudoinverse of $\mathbf{\Lambda}$, suitably truncated prior to inversion in order to exclude singular values λ_m which are zero, or less than some tolerance λ_{tol} . This truncation is the mechanism of regularization in SVD. Of all the solutions $\Delta\sigma$ with minimum error $\|\Delta\mathbf{Z}\|$, it gives the unique solution satisfying the additional constraint of minimum norm $\|\Delta\sigma\|$.

F. Matrix Preconditioning

The matrix \mathbf{S} has greatest sensitivity to voxels nearest the measurement surface. This causes deeper variations to be blurred or not detected, a significant contributor to ill-posedness in physical terms. A similar situation arises in a variety of linear inverse problems, including problems in geophysics [34] and EEG/MEG [15]. A correction scheme is motivated by noting that (13) may always be written

$$\Delta\mathbf{Z} = (\mathbf{S}\mathbf{W})(\mathbf{W}^{-1}\Delta\sigma) \quad (15)$$

provided the matrix \mathbf{W} is nonsingular, i.e., has a unique and well-behaved inverse \mathbf{W}^{-1} . The simplest way to ensure that \mathbf{W} is nonsingular is to make it diagonal

$$\mathbf{W} = \text{diag}(w_k) \quad (16)$$

and require all $w_k \neq 0$. With this weighting scheme, a formal solution may be written as

$$\Delta\sigma \simeq \mathbf{W}(\mathbf{S}\mathbf{W})^+ \Delta\mathbf{Z} \quad (17)$$

where $(\mathbf{S}\mathbf{W})^+$ represents the Moore–Penrose pseudoinverse of $\mathbf{S}\mathbf{W}$. Such a scheme is useful if the problem of inverting the matrix $\mathbf{S}\mathbf{W}$ is less ill-posed than inverting \mathbf{S} .

An effective choice for the w_k normalizes for the total sensitivity in each voxel, by summing over all measurements [15], [34]

$$w_k = \left[\sum_{\mu=1}^M S_{\mu k}^2 \right]^{-1/2}. \quad (18)$$

In EEG/MEG, the inverse problem analogous to (13) involves the lead field matrix \mathbf{L} rather than \mathbf{S} , and a weighting scheme analogous to (15)–(18) is referred to as the “weighted minimum norm” approach [15].

To our knowledge, this weighting scheme has not been applied previously to the EIT inverse problem. We demonstrate

below that weighting increases the number of linearly independent measurements that contribute to the solution, balances the differences between the various measurement patterns, and improves image reconstruction overall.

G. Independent Measurements

We first consider the number of linearly independent measurements M which contribute to \mathbf{S} . One way to count them is the following. Given a total number N_e electrodes, there are at most $N_p \equiv N_e(N_e - 1)/2$ unique electrode pairs available for current injection. Potentials at the injection electrodes are excluded [18], leaving only $(N_e - 2)$ electrodes to measure voltage. Since one electrode must be used as a reference, there are at most $(N_e - 3)$ independent voltage measurements. Taking all injection and measurement pairs gives $M_t = N_p(N_e - 3)$ independent impedance measurements theoretically. For $N_e = 16$ surface electrodes, this implies $N_p = 120$ injection pairs, and a total of $M_t = 1560$ possible measurements.

In most applications, this number is reduced further by invoking the four-electrode reciprocity theorem [19], which states that for any measurement set μ , the mutual impedance Z_μ is preserved under an interchange of injection $\{\text{AB}\}$ and measurement $\{\text{CD}\}$ pairs. This relation is apparent in (6) since $\Delta Z_\mu \rightarrow 0$ as $\Delta\sigma_k \rightarrow 0$. If this reciprocity argument is applied in the OPP measurement pattern (defined below), then effectively there are not N_p but only $N_e/2$ independent injection pairs, resulting in $M_r = (N_e/2)(N_e - 3)$ independent measurements. For $N_e = 16$, this implies $N_e/2 = 8$ injection pairs, and $M_r = 104$ total possible measurements. This simplification speeds data acquisition by a factor of order N_e .

The above argument ignores noise. In practice a variety of EIT measurement schemes appear in the literature [28]. In the “adjacent” or “neighboring” pattern (ADJ), the injection and measurement pairs are each composed of adjacent electrodes, and the two pairs are moved independently around the disc [30]. In the “opposite” or “diametric” pattern (OPP), the injection pairs are composed of diametrically opposed electrodes, but the measurement pairs are composed of adjacent electrodes as before [28].

By ignoring noise, it is possible to apply re-referencing and reciprocity sequentially and show the theoretical equivalence between ADJ and OPP measurement patterns. Yet this equivalence is violated in the presence of instrument noise and background EEG. Indeed, quite a few authors [5], [7], [43]–[45] have noted that the different measurement patterns have different sensitivities, and this choice affects image quality. There have even been efforts to derive optimal measurement schemes. One such scheme assumes a cosine-distributed current injection pattern [45]. For a homogeneous sphere, this has the effect of generating straight equipotential lines through the volume, and casts the EIT problem to be more like X-ray computed tomography (CT), which is soluble. While a sinusoidal current pattern may be applied to any body, it seems unlikely to have the desired effect of generating straight current paths when applied to the highly heterogeneous head.

In what follows, we consider both ADJ and OPP patterns, along with a composite pattern (ALL) based upon $M_t = N_p(N_e - 3)$ measurements. We use SVD to show that \mathbf{S}

has different properties in each case resulting in different severities of ill-posedness. We then show that the above weighting scheme balances the overall sensitivities of these patterns, and improves image quality.

III. NUMERICAL RESULTS

A. Head and Stroke Models

For the purposes of electrical modeling. It is usually assumed that the head is comprised of four tissues: brain, CSF, skull, and scalp, each characterized by a single, scalar conductivity σ . The conductivities of the three soft tissues are essentially agreed upon: brain ($\sigma_b = 0.15$ S/m [12]), CSF ($\sigma_c = 1.8$ S/m [4]), and scalp ($\sigma_t = 0.44$ S/m [12]). We use these values here.

The conductivity σ_s of the living human skull has been the source of much debate. In the most widely cited work on the skull [36], Rush and Driscoll immersed a human skull in a saline tank of known conductivity, and found that the saturated skull had an equivalent conductivity equal to 1/80 that of the immersing fluid. Since then, most three- and four-layer head models in EEG and MEG have assumed $\sigma_b/\sigma_s = 80$ [37], [38], as though the living skull were saturated with brain-like fluid, i.e., rather than CSF-like fluid. Taking $\sigma_b = 0.33$ S/m, this implies $\sigma_s = 0.0042$ S/m, the number commonly used in the literature [38].

It is becoming clear, however, that the skull conductivity has been underestimated for some time [10], [32]. The study by Law [26] suggests an average skull conductivity $\sigma_s = 0.018$ S/m [10], giving $\sigma_b/\sigma_s = 8.33$. Like the Rush and Driscoll finding [36], this result is difficult to interpret because the measured conductivities were highly variable and it is not assured that soaking a dry skull in saline reconstitutes its conductivity accurately (P. Nunez, personal communication). The most reliable skull measurements were made recently on a fresh human cadaver [32], where it was found that on average the skull conductivity $\sigma_s = 0.015$ S/m. This is in rough agreement with [26], implying a similar ratio $\sigma_b/\sigma_s = 10$. The ratio σ_t/σ_s is the main determinant of EIT sensitivity. Taking $\sigma_t = 0.44$ S/m implies $\sigma_t/\sigma_s = 30$. We use $\sigma_s = 0.015$ S/m here.

Fig. 2 shows the finite-element (FE) mesh used for simulations. It includes 1141 nodes and 2166 triangles. Similar to the one used by Bayford *et al.* [5], this mesh has more triangles in the skull layer to better accommodate the steeper potential gradients.

To determine the absolute detection capability of each pattern, we computed the changes in surface potential for five focal anomalies, meant to mimic the conductivity changes associated with ischemic and hemorrhagic stroke. Each anomaly was comprised of 32 elements, with area equal to 5.47 cm². The five regions were numbered in order of increasing depth. The third region is shown as a dark area in Fig. 2. Others were shifted radially by two FEs. The size of the anomalies were fixed in this study, but a more complete study should include dependence on both size and depth.

We assume that ischemic tissue may be characterized by a contiguous region with conductivity equal to 50% that of brain: $\sigma_i = 0.075$ S/m [20]. We assume that a hemorrhage may be characterized by a contiguous region with conductivity equal to

TABLE I
DETECTED $\delta\Phi$ (μV)—HEMORRHAGE

	Adjacent		Opposite		All Pairs	
	max	ave	max	ave	max	ave
R						
1	2.83	0.44	10.65	2.19	14.89	8.30
2	1.52	0.34	7.10	1.85	9.51	5.98
3	0.97	0.29	4.74	1.79	5.89	4.42
4	0.73	0.27	3.72	1.73	4.21	3.50
5	0.64	0.26	3.32	1.71	3.63	2.95

TABLE II
DETECTED $\delta\Phi$ (μV)—ISCHEMIA

	Adjacent		Opposite		All Pairs	
	max	ave	max	ave	max	ave
R						
1	1.36	0.21	5.05	1.03	6.46	3.87
2	0.85	0.17	3.56	0.95	4.73	3.10
3	0.54	0.15	2.48	0.94	2.98	2.31
4	0.40	0.14	1.92	0.91	2.19	1.83
5	0.34	0.14	1.72	0.90	1.89	1.55

that of blood: $\sigma_h = 0.61$ S/m [12]. This assumes that blood completely displaces brain tissue, which is the most common occurrence. It probably does not apply to the case where blood replaces only the extracellular fluid, which would tend to decrease the bulk tissue conductivity, since blood has a lower conductivity than extracellular fluid.

B. Detection Sensitivity

The larger the change in the measured potentials, the more easily an anomaly will be detected above the measurement noise. Tables I and II show the changes in surface potential $\delta\Phi \equiv \Delta\Phi_{\text{CD}}(\sigma + \Delta\sigma) - \Delta\Phi_{\text{CD}}(\sigma)$ for each anomaly, assuming $I_{\text{AB}} = 100$ μA . We compared ADJ, OPP, and ALL patterns. To make a more direct comparison, in the ALL case we report the average over the largest 104 values of $\delta\Phi$ only. (If all 1560 values are considered, then the average $\delta\Phi$ for ALL falls between ADJ and OPP.)

In all cases, the maximum and average $\delta\Phi$ are ordered according to $\text{ADJ} < \text{OPP} < \text{ALL}$. The relation between OPP and ADJ may support some of the statements in [5]. Our restriction to the brain layer prefers OPP over ADJ patterns, which makes intuitive sense because the lead fields in OPP configurations penetrate the brain compartment more deeply and sensitively than ADJ configurations [28]. It stands to reason that restricting to the scalp layer, in contrast, would prefer ADJ over OPP, but this issue is not pursued here.

The fact that the ALL pattern has highest sensitivity suggests it may be possible to select optimal measurement patterns, equivalent to neither OPP nor ADJ, which are particularly sensitive to certain regions of the volume. This argument is much like that made by Gencer *et al.* [13] in the context of optimal EEG reference electrode placement, and is extended here to EIT.

In practice, the detectability of $\delta\Phi$ must be considered in relation to the noise levels. Injecting $I_{AB} = 100 \mu\text{A}$ into our FE model results in $\Delta\Phi_{CD}$ ranging over $\pm 2500 \mu\text{V}$. The acquired signal is assumed to be a sum of the impressed potential $\Delta\Phi_{CD}$ and two additive noise contributions: 1) amplifier noise results in the addition of a Gaussian random variable to each time point [zero-mean and $0.6 \mu\text{V}$ root-mean square (RMS)]; 2) resting EEG contributes a broad-banded signal with amplitude on the order of $10 \mu\text{V}$. By injecting at 100 Hz for 5 s/pair with 250-Hz sampling, then using the FFT to determine amplitude and phase of the impressed potentials, the retrieval error δV is approximately Gaussian and less than $0.01 \mu\text{V}$ RMS. We use this value here, but higher frequencies and better signal analytic techniques could further reduce δV and speed acquisition time.

C. Singular Value Decomposition

To quantify the effect of preconditioning with \mathbf{W} , we computed for \mathbf{S} and \mathbf{SW} the condition number $\text{Cond} \equiv \log_{10}(\lambda_{\max}/\lambda_{\min})$, the maximum singular value λ_{\max} , and the Rank (the number of singular values λ_m greater than some tolerance λ_{tol}) for each pattern, assuming $\sigma_b = 0.15 \text{ S/m}$. To determine λ_{tol} , Press *et al.* [35] suggest using N times the expected noise levels, which would imply $\lambda_{\text{tol}} \simeq 0.001 \Omega^2\text{m}$. We obtained better tomographic reconstructions with $\lambda_{\text{tol}} = 0.01 \Omega^2\text{m}$. (Note that the singular vectors are normalized to unity, so the singular values λ_m carry the units of the matrix.)

Table III shows the results for the unweighted matrix \mathbf{S} . The condition numbers are ordered according to $\text{ADJ} < \text{OPP} < \text{ALL}$, but practically speaking are very similar, always adequate for single-precision computation. The maximum eigenvalue λ_{\max} and Rank are also ordered according to $\text{ADJ} < \text{OPP} < \text{ALL}$, but the effect is much more pronounced. Since the maximum eigenvalue presumably makes the largest contribution to (13) (recall the eigenvectors are normalized to unity), this suggests that the three patterns considered will behave very differently in the presence of noise. This seems to support the claim in [5], that the OPP pattern is preferable to ADJ.

Table IV shows the results for the matrix product \mathbf{SW} . The condition numbers are essentially unchanged, with the exception of OPP, which is possibly not quite inadequate for single-precision computation. The most notable effect is that λ_{\max} and the Rank of \mathbf{SW} are increased significantly relative to those of \mathbf{S} . Since a larger number of singular values and vectors may now contribute meaningfully to the inverse, it seems plausible that the tomographic reconstructions obtained from \mathbf{SW} will be better than those from \mathbf{S} . This is demonstrated clearly for hemorrhage, and to a lesser degree for ischemia.

D. Tomographic Reconstruction

We applied our inverse procedure to ten cases, comprised of hemorrhagic and ischemic anomalies at the five Region locations described in Section III-A. Fig. 3 shows by contour plotting the result for a hemorrhage in Region 3, defined in Fig. 2. The two columns correspond to unweighted (left) and weighted (right) regularization, and the three rows correspond

TABLE III
THE MATRIX \mathbf{S}

	Adjacent	Opposite	All Pairs
Cond	5.13	6.00	6.49
λ_{\max}	0.13	1.00	3.08
Rank	24	34	48

TABLE IV
THE MATRIX \mathbf{SW}

	Adjacent	Opposite	All Pairs
Cond	5.89	7.39	6.60
λ_{\max}	17.9	24.4	23.7
Rank	74	60	66

to the three measurement patterns: ADJ (top), OPP (middle) and ALL (bottom). In all cases the anomaly is clearly visible.

For both weighted and unweighted cases, the ADJ pattern leads to erroneous variations deep in the brain volume. For the unweighted case, this is accompanied by erroneous variations at distant locations of any radius. Most notably, for all unweighted cases, the solution has erroneous variations near the outer brain surface. This is presumably a numerical instability caused by \mathbf{S} having disproportionately high sensitivity there. This defect in the tomographic reconstruction is repaired almost entirely by preconditioning.

To summarize the results for both stroke types and all Regions, we computed the percent correlation

$$\% \text{Corr} = \frac{\sum_k \sigma_k^* \sigma_k^\infty}{\sqrt{\sum_k \sigma_k^*} \sqrt{\sum_k \sigma_k^\infty}} \times 100 \quad (19)$$

between the actual conductivity distribution σ_k^* , and the computed conductivity distribution σ_k^∞ obtained by iterating (10) to convergence. Each iterative solution was initialized with a constant brain conductivity $\sigma_b = 0.15 \text{ S/m}$.

Table V shows the results for the hemorrhage case, which initially has 90.83% correlation. Several consistencies are apparent. First, in all cases, the final correlation is much higher than the initial correlation, demonstrating that the iterative algorithm converged to a more optimal solution. Second, with few exceptions (weighted OPP and ALL, Region 2) the percent correlation is higher for more superficial regions, presumably because the effect of preconditioning is imperfect at rendering the sensitivity equal at all depths. Third, with only one exception (Region 2, ALL), the percent correlation is increased by preconditioning with \mathbf{W} . Together these results imply that cerebral hemorrhage should be detectable and even localizable with these techniques.

Table VI shows the results for the ischemia case, for which the initial correlation is 99.66%. This high initial correlation foreshadows a more challenging imaging problem. In most cases the iterative algorithm converged to a more optimal solution, but the differences in the initial and final correlation values tend to be in the third or fourth significant figure, rather than the second, as was the case for hemorrhage. Overall the effects of Region depth

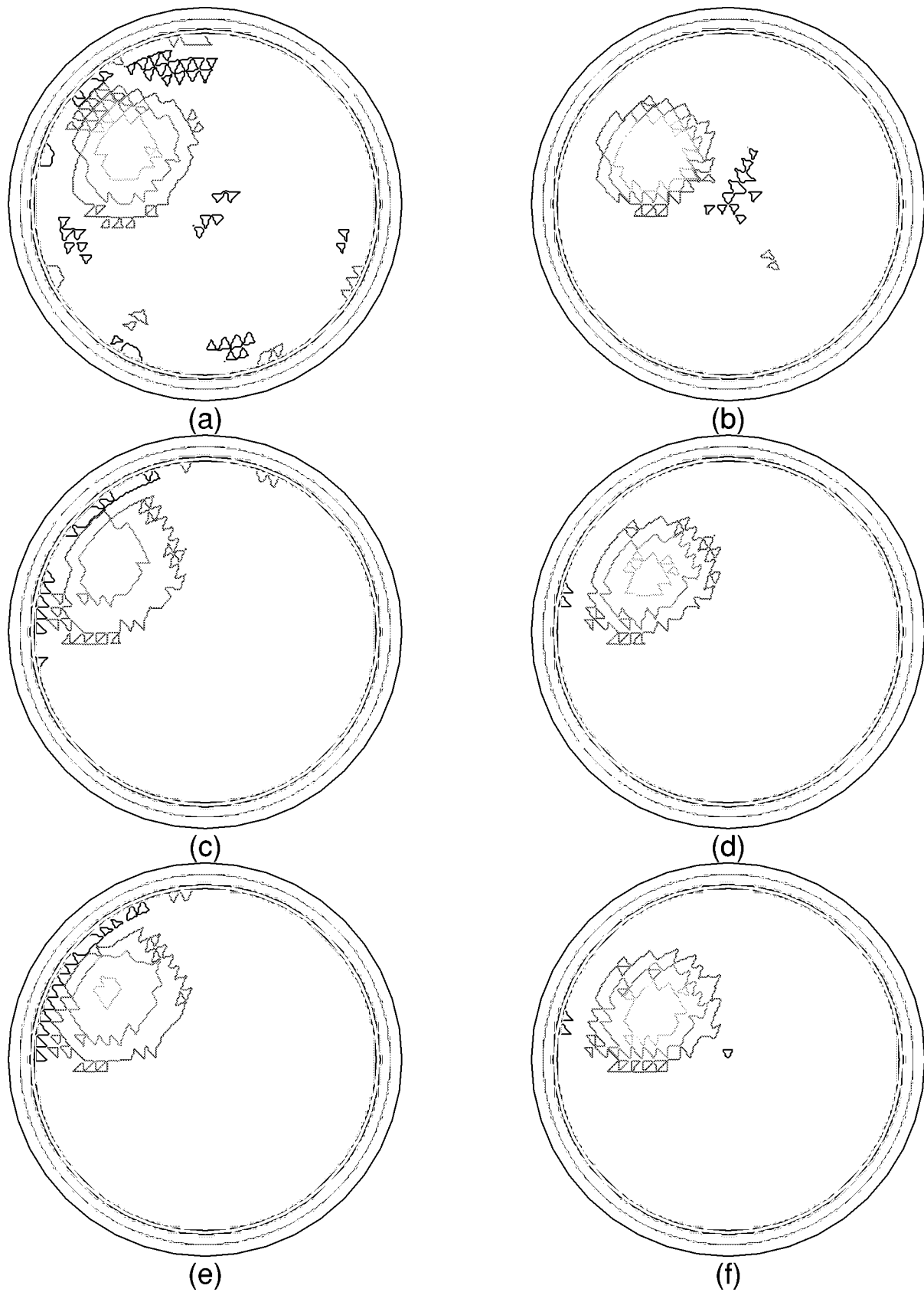


Fig. 3. Tomographic reconstruction of a hemorrhage in Region 3, shown in Fig. 2. Left column is without weighting: (a) adjacent, (c) opposite, and (e) all pairs. Right column is with weighting: (b) adjacent, (d) opposite, and (f) all pairs.

and weighting with W are minimal for ischemia. With few exceptions, the more superficial Regions are more readily imaged,

but the effects of weighting are negligible, and not even consistently an improvement. Evidently, ischemia is a much more

TABLE V
PERCENT CORRELATION—HEMORRHAGE

R	Adjacent		Opposite		All Pairs	
	S	SW	S	SW	S	SW
1	95.95	97.51	95.41	96.61	95.55	97.22
2	94.31	95.52	92.91	93.16	93.47	92.89
3	92.49	94.51	92.40	93.23	92.75	93.46
4	92.91	94.43	91.64	92.63	91.84	93.11
5	92.64	94.16	91.62	92.12	91.97	93.18

TABLE VI
PERCENT CORRELATION—ISCHEMIA

R	Adjacent		Opposite		All Pairs	
	S	SW	S	SW	S	SW
1	99.75	99.73	99.88	99.87	99.89	99.86
2	99.72	99.80	99.78	99.76	99.80	99.72
3	99.71	99.66	99.74	99.77	99.76	99.76
4	99.72	99.66	99.70	99.75	99.72	99.75
5	99.58	99.69	99.70	99.73	99.73	99.75

challenging problem than hemorrhage, at least for the parameter values employed here. Because the potential changes in Table II are easily measurable, however, it seems clear that ischemic changes should be detectable in practice. Furthermore, because the iterative algorithm usually converges to a more optimal solution, it seems promising that ischemic tissue could also be approximately localized, especially with better techniques. Suggestions for improvements are given in the Discussion.

Surprisingly, even in the hemorrhage case, for which the improvements are visible, the correlation function does not exhibit a consistent improvement for ALL and OPP patterns over the ADJ pattern, even though such an improvement is clearly visible in Fig. 3. This may be because the correlation treats the two conductivity distributions as vectors with mutually orthogonal components, and gives identically zero contribution if the correct conductivity is obtained at a neighboring element, no matter how nearby. Other measures of image similarity should be studied to allow reliable interpretations based upon purely numerical measures.

IV. DISCUSSION

We have used a standard iterative approach to solve the EIT inverse problem for brain anomalies, assuming that the other tissue conductivities are known. Inversion and regularization were accomplished using SVD techniques. To improve regularization, however, we introduced a matrix preconditioning step that accounts for the depth dependence of the sensitivity matrix \mathbf{S} , which is biased toward the measurement surface. To our knowledge this has not been applied previously in EIT. We demonstrated the effects on the condition number, largest singular value, and rank of \mathbf{S} , and found that more independent measurements enter meaningfully into the inverse solution with

preconditioning. This improves image quality overall, as seen in the right column of Fig. 3.

We applied the technique to ischemic and hemorrhagic stroke, using plausible values for the associated changes in brain conductivity. For hemorrhage, the anomaly is easily detected, and the dependencies on measurement pattern and preconditioning are partly understandable in terms of the rank of the sensitivity matrix. For ischemia, the anomaly appears detectable, and the dependences on measurement pattern and preconditioning are far less pronounced. This could be partly due to our choice of stopping criterion (11), which may stop the iteration prematurely for ischemia but not hemorrhage, since percent correlation for ischemia is so high initially. More studies are necessary to determine objective criteria for stopping the iteration, as well as for regularization performed at each iteration step.

Clearly a 2-D, geometrically perfect head model is an idealization. This approach should be extended to 3-D. The FEM will allow for correct head geometry. Errors in head geometry will lead to systematic differences between measured and computed values of the mutual impedance Z_{μ} but, if geometry is included consistently, then reasonably good localization may presumably be obtained. A more difficult question is how to obtain good baseline conductivity values for each of the head tissues. The simplest way is a four-parameter approach [10], which is overdetermined by design. Local variations in the tissue conductivities, especially in the skull, will lead to systematic errors in computing the lead fields and thereby the sensitivity matrix. This would most likely lead to localization errors, but still permit reliable detection, and that alone may be enough to positively impact clinical brain and stroke monitoring.

Many extensions are possible, which should improve tomographic reconstruction. Practically speaking, using more electrodes will make the sensitivity matrix more square. Algorithmically, the present approach is equivalent to the weighted minimum norm algorithm used commonly in EEG and MEG, but other methods exist which have yet to be applied to EIT, e.g., the FOCUSS algorithm [15], which solves the EEG/MEG linear inverse problem by starting with the weighted minimum norm solution, then iterating to sharpen the image. This approach seems particularly well suited for stroke detection, since stroke is usually characterizable as a single, contiguous region. A further improvement, applicable to both the estimation of baseline conductivity values as well as stroke monitoring, may be to cast the static EIT problem inverse problem in a Bayesian framework, which includes prior information about likely conductivity values, stabilizing the inverse solutions.

ACKNOWLEDGMENT

The authors thank Dr. O. Portniaguine at the Scientific Computing and Imaging Institute, University of Utah, for helpful discussions.

REFERENCES

- [1] G. W. Albers, J. D. Easton, R. L. Sacco, and P. Teal, "Antithrombotic and thrombolytic therapy for ischemic stroke," *Chest*, vol. 114, pp. 683S–698S, 1998.

- [2] K. A. Awada, D. R. Jackson, S. B. Baumann, J. T. Williams, D. R. Winton, P. W. Fink, and B. R. Prasky, "Effect of conductivity uncertainties and modeling errors on EEG source localization using a 2-D model," *IEEE Trans. Biomed. Eng.*, vol. 45, pp. 1135–1145, Sept. 1998.
- [3] P. A. Barber, D. G. Darby, P. M. Desmond, Q. Yang, R. P. Gerraty, D. Jolley, G. A. Donnan, B. M. Tress, and S. M. Davis, "Prediction of stroke outcome with echoplanar perfusion- and diffusion-weighted imaging," *Neurology*, vol. 51, pp. 418–426, 1998.
- [4] S. B. Baumann, D. R. Wozny, S. K. Kelly, and F. M. Meno, "The electrical conductivity of human cerebrospinal fluid at body temperature," *IEEE Trans. Biomed. Eng.*, vol. 44, pp. 220–223, Mar. 1997.
- [5] R. H. Bayford, K. G. Boone, Y. Hanquan, and D. S. Holder, "Improvement of the positional accuracy of EIT images of the head using a Lagrange multiplier reconstruction algorithm with diametric excitation," *Physiol. Meas.*, vol. 17, pp. A49–A57, 1996.
- [6] K. G. Boone, "The possible use of applied potential tomography for imaging action potentials in the brain," Ph.D. dissertation, University of London, 1995.
- [7] M. Cheney, D. Isaacson, and J. C. Newell, "Electrical impedance tomography," *SIAM Rev.*, vol. 41, no. 1, pp. 85–101, 1999.
- [8] B. M. Eyuboglu, T. C. Pilkington, and P. D. Wolf, "Estimation of tissue resistivities from multiple-electrode impedance measurements," *Phys. Med. Biol.*, vol. 39, pp. 1–17, 1994.
- [9] T. C. Ferree, M. T. Clay, and D. M. Tucker, "The spatial sensitivity of scalp EEG," *Neurocomputing*, vol. 38–40, pp. 1209–1216, 2001.
- [10] T. C. Ferree, K. J. Eriksen, and D. M. Tucker, "Regional head tissue conductivity estimation for improved EEG analysis," *IEEE Trans. Biomed. Eng.*, vol. 47, pp. 1584–1592, Dec. 2000.
- [11] K. R. Foster and H. P. Schwan, "Dielectric properties of tissues and biological materials: A critical review," *Critical Reviews in Biomed. Eng.*, vol. 17, no. 1, pp. 25–104, 1989.
- [12] L. A. Geddes and L. E. Baker, "The specific resistance of biological materials: A compendium of data for the biomedical engineer and physiologist," *Med. Biol. Eng.*, vol. 5, pp. 271–293, 1967.
- [13] N. G. Gencer, S. J. Williamson, A. Gueziec, and R. Hummel, "Optimal reference electrode selection for electric source imaging," *Electroenceph. Clin. Neurophys.*, vol. 99, pp. 163–173, 1996.
- [14] D. B. Geselowitz, "An application of electrocardiographic lead theory to impedance plethysmography," *IEEE Trans. Biomed. Eng.*, vol. 18, pp. 38–41, Jan. 1971.
- [15] I. F. Gorodnitsky, J. S. George, and B. D. Rao, "Neuromagnetic source imaging with FOCUSS: A recursive weighted minimum norm algorithm," *Electroenceph. Clin. Neurophysiol.*, vol. 95, pp. 231–251, 1995.
- [16] J. H. Hansen and C. E. Olsen, "Brain extracellular space during spreading depression and ischemia," *Acta. Physiol. Scand.*, vol. 108, pp. 355–365, 1989.
- [17] J. Haueisen, C. Ramon, M. Eiselt, H. Brauer, and H. Nowak, "Influence of tissue resistivities on neuromagnetic fields and electric potentials studied with a finite-element model of the head," *IEEE Trans. Biomed. Eng.*, vol. 44, pp. 727–735, Aug. 1997.
- [18] C. A. Heiland, *Geophysical Exploration*. Englewood Cliffs, NJ: Prentice-Hall, 1940.
- [19] H. L. F. Helmholtz, "Ueber einige Gesetze der Vertheilung elektrischer Ströme in körperlichen Leitern mit Anwendung auf die thierisch-elektrischen Versuche," *Ann. Physik und Chemie*, vol. 89, pp. 211–233, 354–377, 1853.
- [20] D. S. Holder, "Detection of cerebral ischemia in the anaesthetized rat by impedance measurement with scalp electrodes: Implications for non-invasive imaging of stroke by electrical impedance tomography," *Clin. Phys. Physiol. Meas.*, vol. 13, pp. 63–76, 1992.
- [21] —, "Electrical impedance tomography with cortical or scalp electrodes during global cerebral ischemia in the anaesthetized rat," *Clin. Phys. Physiol. Meas.*, vol. 13, pp. 87–98, 1992.
- [22] D. H. Ingvar, B. Sjolund, and A. Ardo, "Correlation between dominant EEG frequency, cerebral oxygen uptake and blood flow," *Electroenceph. Clin. Neurophys.*, vol. 41, pp. 405–420, 1976.
- [23] J. D. Jackson, *Classical Electrodynamics*. New York: Wiley, 1975.
- [24] D. D. Jackson, "Interpretation of inaccurate, insufficient and inconsistent data," *Geophys. J. Roy. Astr. Soc.*, vol. 28, pp. 97–109, 1972.
- [25] K. Jerbi, W. R. B. Lionheart, P. J. Vauhkonen, and M. Vauhkonen, "Sensitivity matrix and reconstruction algorithm for EIT assuming axial uniformity," *Physiol. Meas.*, vol. 21, pp. 61–66, 2000.
- [26] S. K. Law, "Thickness and resistivity variations over the upper surface of the human skull," *Brain Topogr.*, vol. 6, no. 2, pp. 99–109, 1993.
- [27] J. Lehr, "A vector derivation useful in impedance plethysmographic field calculations," *IEEE Trans. Biomed. Eng.*, vol. BME-19, pp. 156–157, Feb. 1972.
- [28] J. Malmivuo and R. Plonsey, *Bioelectromagnetism*. New York: Oxford Univ. Press, 1995.
- [29] S. Meeson, A. L. T. Killingback, and B. H. Blott, "The dependence of EIT images on the assumed initial conductivity distribution: A study of pelvic imaging," *Phys. Med. Biol.*, vol. 40, pp. 643–657, 1995.
- [30] T. Murai and Y. Kagawa, "Electrical impedance computed tomography based on a finite-element model," *IEEE Trans. Biomed. Eng.*, vol. BME-32, pp. 177–184, 1985.
- [31] K. Nagata, "Topographic EEG in brain ischemia—Correlation with blood flow and metabolism," *Brain Topogr.*, vol. 1, no. 2, pp. 97–106, 1988.
- [32] T. F. Oostendorp, J. Delbeke, and D. F. Stegeman, "The conductivity of the human skull: Results from *in vivo* and *in vitro* measurements," *IEEE Trans. Biomed. Eng.*, vol. 47, pp. 1487–1492, Nov. 2000.
- [33] R. Plonsey, *Bioelectric Phenomena*. New York: McGraw-Hill, 1969.
- [34] O. N. Portniaguine, "Image focusing and data compression in the solution of geophysical inverse problems," Ph.D. dissertation, Dept. Geology Geophys., Univ. Utah, Salt Lake City, 1999.
- [35] W. H. Press, S. A. Teukolsky, W. T. Vetterling, and B. P. Flannery, *Numerical Recipes in C*. New York: Cambridge Univ. Press, 1992.
- [36] S. Rush and D. A. Driscoll, "Current distribution in the brain from surface electrodes," *Anesthesia and Analgesia*, vol. 47, no. 6, pp. 717–723, 1968.
- [37] —, "EEG electrode sensitivity—An application of reciprocity," *IEEE Trans. Biomed. Eng.*, vol. 16, pp. 15–22, Jan. 1969.
- [38] C. J. Stok, "The influence of model parameters on EEG/MEG single dipole source estimation," *IEEE Trans. Biomed. Eng.*, vol. BME-34, pp. 289–296, Apr. 1987.
- [39] T. Tidswell, A. Gibson, R. H. Bayford, and D. S. Holder, "Three-dimensional electrical impedance tomography of human brain activity," *NeuroImage*, vol. 13, pp. 283–294, 2001.
- [40] A. T. Tidswell, A. Gibson, R. H. Bayford, and D. S. Holder, "Validation of a 3D reconstruction algorithm for EIT of human brain function in a realistic head-shaped tank," *Physiol. Meas.*, vol. 22, pp. 177–185, 2001.
- [41] P. Tong and J. N. Rossettos, *Finite-Element Method: Basic Technique and Implementation*. Cambridge: MIT Press, 1977.
- [42] M. J. Van Burik and M. J. Peters, "Estimation of the electric conductivity from scalp measurements: Feasibility and application to source localization," *Clinical Neurophysiology*, vol. 111, pp. 1514–1521, 2000.
- [43] P. J. Vauhkonen, M. Vauhkonen, T. Savolainen, and J. P. Kaipio, "Three-dimensional electrical impedance tomography based on the complete electrode method," *IEEE Trans. Biomed. Eng.*, vol. 46, pp. 1150–1160, Sept. 1999.
- [44] J.-Z. Wang, S. J. Williamson, and L. Kaufman, "Magnetic source images determined by a lead-field analysis: The unique minimum-norm least-squares estimation," *IEEE Trans. Biomed. Eng.*, vol. 39, pp. 665–675, July 1992.
- [45] T. J. Yorkey, "Electrical impedance tomography with piecewise polynomial conductivities," *J. Comp. Phys.*, vol. 91, pp. 344–360, 1990.
- [46] M. Zadehkoochak, B. H. Blott, T. K. Hames, and R. F. George, "Spectral expansion analysis in electrical impedance tomography," *J. Phys. D: Appl. Phys.*, vol. 24, pp. 1911–1916, 1991.